



Contents lists available at ScienceDirect

Computer Vision and Image Understanding

journal homepage: www.elsevier.com/locate/cviu

Measuring 3D shape similarity by graph-based matching of the medial scaffolds

Ming-Ching Chang^{a,*}, Benjamin B. Kimia^b^a Visualization and Computer Vision Lab (VCV), General Electric Global Research Center, Niskayuna, NY, USA^b Laboratory for Engineering Man/Machine Systems (LEMS), Division of Engineering, Brown University, Providence, RI, USA

ARTICLE INFO

Article history:

Received 16 February 2010

Accepted 11 October 2010

Available online xxx

Keywords:

Medial axis
 Medial scaffold
 Transition
 3D shape similarity
 Hypergraph matching
 3D shape matching
 3D shape retrieval

ABSTRACT

We propose to measure 3D shape similarity by matching a medial axis ($\mathcal{M}A$) based representation—the *medial scaffold* ($\mathcal{M}S$). Shape similarity is measured as the minimum extent of deformation necessary for one shape to match another, guided by representing the shapes using the $\mathcal{M}S$. This approach is an extension of an approach to match 2D shapes by matching their *shock graphs*, whereas here in 3D the $\mathcal{M}S$ is in an extended form of a hypergraph. The $\mathcal{M}S$ representation is both hierarchical and complete. Our approach approximates the theoretical optimal deformation path between two shapes by modeling shape deformations as discrete topological changes (the *transitions*) of the $\mathcal{M}S$ hypergraphs, where each graphical transition is associated with a cost measurement defined by the transition. Our algorithm first regularizes the $\mathcal{M}S$ hypergraphs and uses the *graduated assignment* graph-matching scheme to match the hypergraphs. A set of compatibility functions is defined to measure the pairwise similarity between the $\mathcal{M}S$ nodes, curves (graph links), and sheets (hyperlinks). Results on matching carpal bones and shapes from the SHREC'10 non-rigid dataset promise its potential in a range of applications.

© 2010 Elsevier Inc. All rights reserved.

1. Introduction

Measuring 3D shape similarity is an important task in object recognition; applications include shape retrieval and clustering in databases [26], querying industrial parts [38], matching bio-chemical structures [6] and others. Central to this task is the issue of shape **representation**. Typically a *descriptor* is extracted from the shape, usually with a great deal of simplification to enable efficient matching. The choice of descriptor is often domain-specific and could vary largely from one application to another, facing the dilemma of either being too coarse (ignoring information) or too complex (redundant and unstable). As the problem of matching *rigid closed* shapes is generalized into matching *partial* or *articulated* shapes, developing a *generic* 3D shape representation for matching and recognition becomes significant and is the primary goal of this paper.

A major branch in shape representation is the symmetry-based **medial axis** ($\mathcal{M}A$) representation [59,12]. The $\mathcal{M}A$ is promising for shape recognition [55,60] in that (i) it organizes the shape information in a *hierarchical, intrinsic* graph-like structure [44], which enables matching parts of deformed shapes naturally, and (ii) such information captured with the $\mathcal{M}A$ is *complete* in that a full shape reconstruction is always possible [29]. Despite these advantages, the $\mathcal{M}A$ is generally sensitive to perturbation and difficult to mod-

el in the 3D case [4]. Such issues have been recently addressed [31,30]. In this paper, we adopt the **Medial Scaffold** ($\mathcal{M}S$)—a hierarchical organization of the 3D $\mathcal{M}A$ into a *hypergraph* form [44] and a *regularization* framework of the $\mathcal{M}S$ [15] to deal with the above barriers. The $\mathcal{M}A$ instabilities which induce sudden topological changes are formally classified as a set of *transitions* and thus can be regularized via a set of *transforms* [15]. We propose to match the regularized $\mathcal{M}S$ such as the ones shown in Fig. 1 to estimate a global similarity between shapes.

Our main contribution is a novel solution to measure 3D shape similarity by matching the $\mathcal{M}S$ hypergraphs representing the underlying shapes. Following a theoretical framework to measure shape similarity as the *minimum deformation* necessary for one shape to match the other in 2D [55], the matching here is guided by the $\mathcal{M}S$ as a representation, which retains both key benefits of the $\mathcal{M}A$ (*hierarchical* and *complete*). The amount of shape deformation can be formulated as an integration of *infinitesimal elastic* changes to optimally match the $\mathcal{M}S$ branches (sheets and curves). Fig. 2a illustrates an example. Since the shape space to explore across matching two arbitrary shapes is huge [55], we propose to approximate this optimal solution by first regularizing the $\mathcal{M}S$ hypergraphs [15] and matching them [16,32]. Two improvements are significant in our approach. First, we propose a natural extension of a popular graph-matching scheme—Gold and Rangarajan's *graduated assignment* graph matching algorithm [32]—to match *hypergraphs*. Second, we define a set of similarity measures to reflect the *structural* and *parametric* differences of free-form 3D shapes represented using the $\mathcal{M}S$ hypergraphs.

* Corresponding author.

E-mail addresses: changm@ge.com, mcchang@lems.brown.edu (M.-C. Chang).

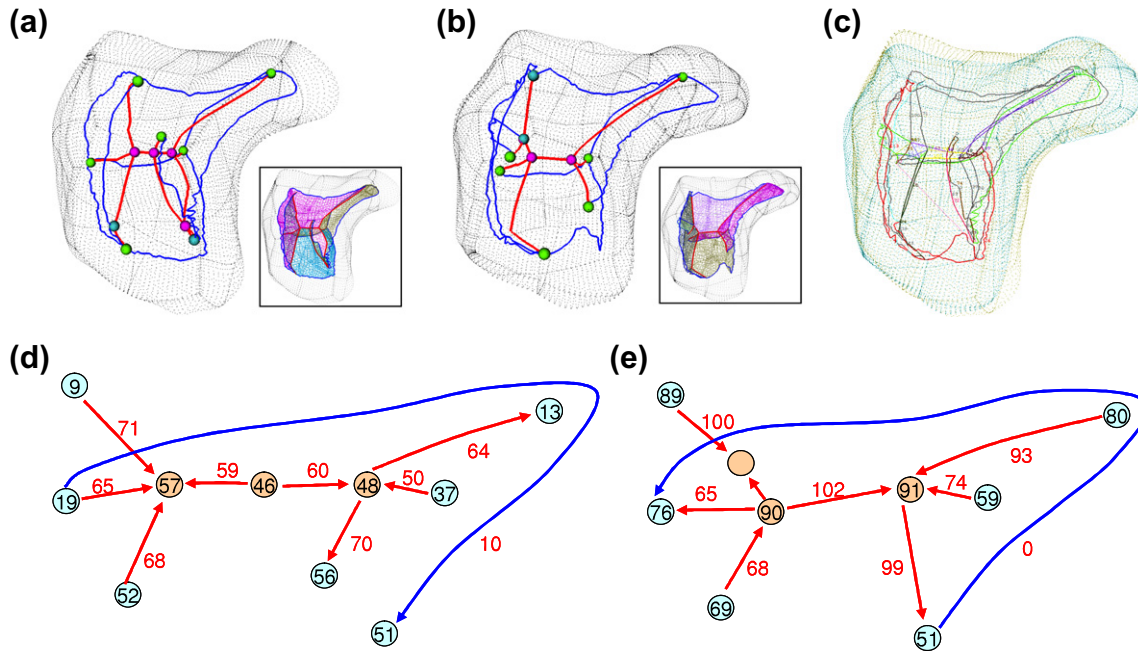


Fig. 1. The matching of the MS hypergraphs of two carpal bones [47] in (a) and (b) is shown in (c). (d and e) show a manual correspondence, where the graph components are labeled with identification numbers. The example in this figure serves as the ground truth to validate and illustrate our automatic matching approach throughout this paper.

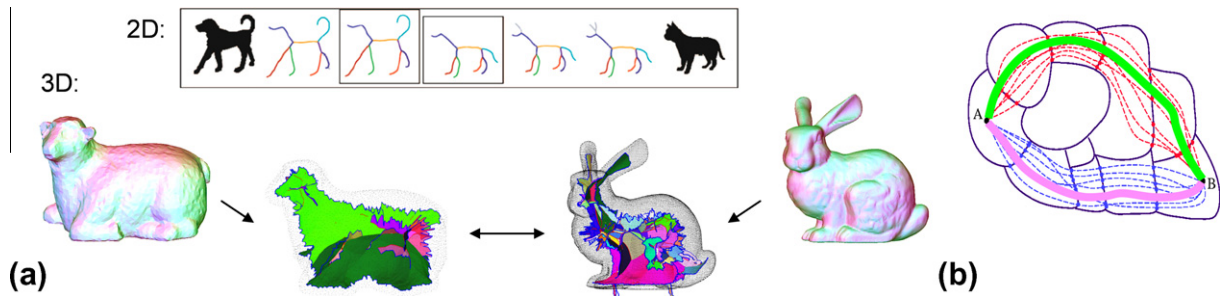


Fig. 2. (a) The *shock graph* in 2D and the MS in 3D as the representation for finding the optimal deformation in matching two shapes. The medial scaffold is the analogy of the *shock graph* in 2D which serves as our representation for searching for optimal deformation of 3D shapes. (b) Deformation path represented as a sequence of discrete *shock transitions*. Each blob represents a *shape cell* [55] where all shapes share a common *shock/MS* topology.

In order to match the regularized MS node produced by repeatedly applying the MS transforms described in [15], we inevitably encounter scenarios in evaluating the similarity between high-order MS nodes produced in the regularization process. These newly discovered scenarios are not covered in Giblin and Kimia's theoretical analysis [31]. Another contribution of this paper is to generalize the classification of the five types of generic MA nodes (namely, $A_1^2, A_1^3, A_3, A_1^4, A_1A_3$) discovered by Giblin and Kimia into two sets of high-order nodes (namely, $A_1^m A_3$ and A_1^n); refer to Section 5.1 for details.

The paper is organized as follows. Section 2 reviews the background in 3D shape similarity matching. Section 3 describes the MS as our representation for 3D shapes. Section 4 covers our extended graph-matching scheme, and Section 5 elaborates the compatibility measures between the MS hypergraph components (nodes, curves, sheets). After the matching is performed, Section 6 computes the final similarity measure by summing up the compatibility measures weighted by the assignment coefficients. Finally, our approach is examined in Section 8 on matching medical shapes (carpal bones), synthetic shapes, and the 200 shapes from the SHREC'10 non-rigid dataset [45].

2. Background

Measuring shape similarity in recognition is a fundamental problem with an abundant literature; refer to [13,25,66] for surveys in the 3D domain. We briefly organize recent approaches into two main categories, namely, the (i) *shape descriptor*-based and (ii) *structural graph*-based methods.¹

Descriptor-based methods are the current mainstream. A shape descriptor (feature, signature) is extracted to describe the shape and distinguish it from others. A large variety of descriptors have been proposed, which are briefly classified into four sub-categories: (i) *local* feature based, which relies on local salient geometric features [28,39] such as the curvature or primitives of flat regions [37,53]; (ii) *global* feature based including spherical functions [40,50,52], shape histogram [2], shape context [5,41], statistical measure-based, such as the shape distribution [49] and generalizations [46,48], coarse-to-fine canonical forms [70], and the recent isometric deformation model [63]. (iii) *view*-based, by matching

¹ Methods 'hybrid' in nature are classified to the most relevant category.

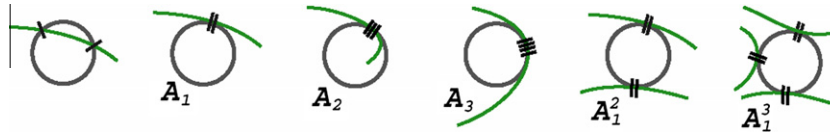


Fig. 3. (From [30, Fig. 3].) Illustration of the notation A_k^n based on contact of curves with a circle in 2D [30]; $k + 1$ counts order of contact (indicated by straight short dark segments); e.g., A_1 is regular tangent contact, A_2 is regular “curvature” contact, A_3 is a curvature maximum contact. The superscript n counts the number of contact points, so that A_1^2 means two A_1 contacts. A similar definition holds for the contact of surfaces with spheres in 3D.

2D views of the 3D objects, including the elevation descriptor [57], aspect-transition descriptor [43], adaptive views clustering [3], the light-field descriptor [18], aspect graph [23], and the recent bag-of-densely-sampled local visual features [27]; and (iv) voxel-based, assuming the input is a solid volume where a distance transform can be effectively computed [40].

Graph-based methods employ a graph to represent the connectivity between *parts* of a shape, where the matching of partial or deformed shapes can be carried out naturally. Recent works are organized by the type of graph used in the methods as follows: (i) the *Reeb graph* is a topological graph based on the Morse analysis on a pre-defined function (such as the geodesic or height functions), where graph edges are not necessarily skeletal/symmetric [9,34,8,10]; (ii) the *skeletal graph* such as [65,7] encodes topological signature vectors for matching; (iii) the *curve-skeleton* is an one-dimensional centerline roughly central inside the 3D shape. Although the curve-skeleton has a much simpler structure in comparing to the \mathcal{MA} (which consists of 2D sheets), a suitable mathematical definition for such “centredness” still needs investigation [20–22,24]; (iv) two-dimensional *medial sheets*: Pizer *et al.* pioneer in using fixed-topology medial models for segmentation [64]; Siddiqi *et al.* [60] employ a directed acyclic graph of the *medial sheets* to retrieve articulated 3D models. Our approach belongs to this category. One significance of our method in comparison to Siddiqi *et al.*'s is that we explicitly exploit of the medial sheet connectivity and singularity structure [15] to extract a 3D graph-like structure for matching. Our approach is a direct extension from a simplified 2D analysis along the line of work in [55,56].

We note that our method is one of a few that is capable of handling *partial*, *non-closed*, and *sampled* shapes. Other methods with such capability include Furuya and Ohbuchi's bag-of-densely-sampled visual features [27], Johnson and Hebert's *spin-image* [39] and a few others [37,53,28], however with restrictions based on respective descriptors in each case. Our claim of the capability to handle partial, non-closed, sampled shapes comes straight from the \mathcal{MS} computation in [17,15] which we rely on. The \mathcal{MS} can be computed and extracted from point-sampled shapes where the sampling is not necessarily uniform. We impose no assumption that the shape is closed (watertight) or complete (*i.e.*, we tolerate missing samples of chunks of shape) when we compute and regularize the \mathcal{MS} . Thus in this work we inherit the above generality in dealing with matching shapes with less constraints.

3. Medial Scaffold (\mathcal{MS}) as shape representation

The 3D medial axis (\mathcal{MA}) generally consists of medial sheets (A_1^2), curves (A_3, A_1^3), and nodes (A_1A_3, A_1^4) [30], where the A_k^n notation [30] indicates the order (k) of contact of a maximal ball with n surface points used to classify the \mathcal{MA} points (Fig. 3). An A_1^3 curve (red in Fig. 4) delimits A_1^2 sheets at an *axis* and ends at A_1^4 or A_1A_3 nodes. An A_3 curve (blue) delimits an A_1^2 sheet at a *rib* and ends at A_1A_3 nodes.

We represent the 3D \mathcal{MA} as the *Medial Scaffold* (\mathcal{MS}) [44,15], which as well organize the abundant information of shape into a hierarchical *hypergraph* form, see Fig. 4. The \mathcal{MS} has several advantages in modeling 3D shapes: (i) shape information is organized *intrinsically* with the \mathcal{MS} structure and is *complete* (in allowing a

full reconstruction of the shape). (ii) Instabilities of the \mathcal{MA} can be formally handled as *transitions* [31], which are sudden \mathcal{MA} topological changes corresponding to perturbation of shape. In 3D there are 7 generic *transitions*, which can be regularized case-by-case via 11 *transforms* defined in [15]. The regularized \mathcal{MS} then captures salient structures of the shape in a simplified form, which is ready to use in subsequent process such as the matching and recognition of shapes. (iii) The \mathcal{MS} can be further reduced into a succinct one-dimensional *graph* like structure by keeping the 2D sheet topology at the medial curves (and compress geometry information), which enables to adopt an efficient graph-based algorithm for matching. (iv) Finally, general practical data such as unorganized points or partial meshes can be handled without restrictions [15].

In this paper, we assume that the \mathcal{MS} of each shape is computed and properly regularized. We propose a graph-matching solution to estimate shape similarity by summing up component-wise compatibilities. To this end, we are essentially using the \mathcal{MS} transitions and transforms as a mean to match shapes. In 2D, the \mathcal{MA} transitions are exploited to annotate the shape which lead to a solution to navigate through the ‘edits’ of \mathcal{MA} topologies (Fig. 2) in exploring candidate deformation paths in matching two shapes. This is the key underlying the concept of Sebastian and Kimia [55] where instabilities or transitions of the medial axis actually document and represent paths of deformation. The recognition system based on this is superb and remains state of the art. In this paper we propose to extend this idea in 3D. Instead of matching the skeletal graph itself, we define a **dissimilarity** measure to reflect the *optimal* deformation cost between two shapes. The computational cost to explore all possible edits to match two \mathcal{MS} hypergraphs is high [14], we thus refer to a *sub-optimal* solution. We first regularize the \mathcal{MS} hypergraphs to capture the *qualitative structure* of the shape and adopt a graph-matching scheme.

Fig. 5 illustrates the proposed approach in computing the similarity of shapes by matching their regularized skeletal graphs. The error between the true distance (dissimilarity) between two shapes $d[\gamma_0, \bar{\gamma}_0]$ and the approximated distance $d[\bar{\gamma}_2, \bar{\gamma}_2]$ is bounded by the triangular inequality of the distance metric.

$$d[\gamma_0, \bar{\gamma}_0] - d[\bar{\gamma}_2, \bar{\gamma}_2] \leq (\varepsilon_{01} + \bar{\varepsilon}_{01} + \varepsilon_{12} + \bar{\varepsilon}_{12}), \quad (1)$$

where ε_{01} , $\bar{\varepsilon}_{01}$, ε_{12} , and $\bar{\varepsilon}_{12}$ are the distances between shapes before/after regularization.² If we assume that (i) the shape regularization is optimal toward simplification (*i.e.*, ε_{01} , $\bar{\varepsilon}_{01}$, ε_{12} , and $\bar{\varepsilon}_{12}$ belongs to the optimal deformation path between γ_0 and $\bar{\gamma}_0$), and (ii) the matching of $(\bar{\gamma}_2, \bar{\gamma}_2)$ is also optimal, the true distance between the original shapes $d[\gamma_0, \bar{\gamma}_0]$ can be approximated by

$$d[\gamma_0, \bar{\gamma}_0] \cong d[\bar{\gamma}_2, \bar{\gamma}_2] + (\varepsilon_{01} + \bar{\varepsilon}_{01} + \varepsilon_{12} + \bar{\varepsilon}_{12}). \quad (2)$$

4. Graph matching the \mathcal{MS} hypergraphs

Graphs are powerful data structures useful in matching and recognition [19]. The computational intractability of graph matching

² Refer to [14, Ch. 8] for a proof of Eq. (1).

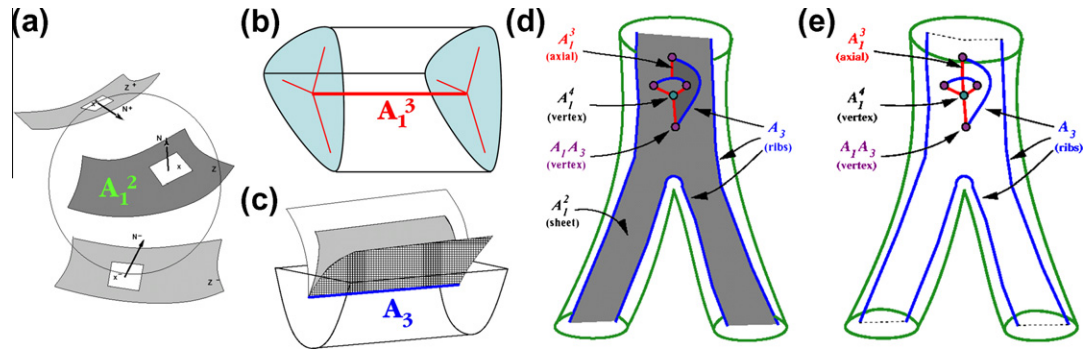


Fig. 4. (From [44, Fig. 5].) Summary of the five generic types of 3D \mathcal{MA} points [30,44]: (a) Each point on an A_1^2 sheet is the center of a sphere with two ordinary A_1 contacts. (b) Each point on an A_1^3 axial curve is the center of a sphere with three ordinary A_1 contacts; this is where three sheets come together. (c) Each point on an A_3 rib curve is a limiting case of two A_1^2 points coming in unison; it corresponds to the ‘boundary’ of the \mathcal{MA} sheet which is associated to the *ridges* on the shape boundary. The five generic types are illustrated on a \mathcal{MS} hypergraph in (d) and in (e) with the medial sheets implicit to emphasize its graph structure.

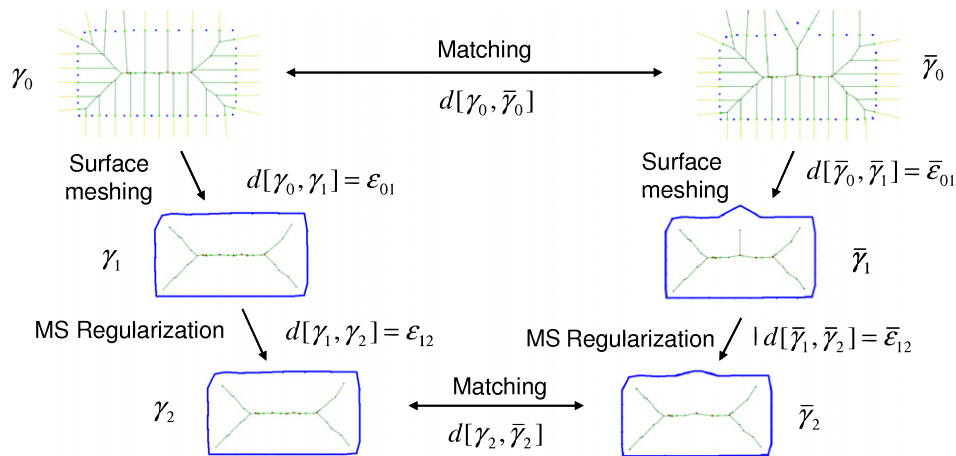


Fig. 5. Schematic illustration of our approach to measure the similarity between two (sampled) shapes by regularization and matching of their skeletal graphs. The similarities measured obtained from this approach is bounded and approximated following the regularization deformation path [14, Ch. 8].

has led to the development of several classes of sub-optimal algorithms, including *search-oriented* methods using heuristics to explore the state space [42], and nonlinear optimization methods such as *relaxation labeling* [36]. Other graph matching approaches include eigenvalue decomposition [67], neural networks [61], linear programming [1], Lagrangian Relaxation [51], and indexing the graph spectra [58], etc.

The *graduated assignment* (\mathcal{GA}) [32] is a relaxation-based energy-minimizing graph matching algorithm suitable to integrate with our approach. We adopt it to match the \mathcal{MS} 's for several reasons: (i) It enforces a *two-way* assignment via “*softassign*” [62], in contrast to *relaxation labeling* which enforces only an one-way assignment. It is extensible to a *three-way* assignment to match the hypergraphs, a strong fit in our case (Section 5.3). (ii) It avoids poor local minimum by a *graduated convexity* continuation technique [11,69], partly due to an explicit encoding of sparsity. The \mathcal{GA} is thus an order of magnitude better than relaxation labeling. (iii) It handles missing/extra nodes and links to stabilize the matching under noisy conditions, a factor essential in matching shapes. (iv) The formulation can be adapted to take into account shape deformations represented by continuous variables. The \mathcal{GA} is thus superior in this regard to the original relaxation labeling and Lagrangian relaxation [32]. (v) Finally, the computational time is comparable to other graph matching techniques reported in [32].

4.1. A review of the \mathcal{GA} graph matching algorithm

We briefly review Gold and Rangarajan's graduated assignment graph matching algorithm [32] in this section. The basic setup of

the \mathcal{GA} is to associate the nodes in two graphs G and \bar{G} by a *match matrix* \mathbf{M} , where 1 represents a match of two nodes and 0 otherwise, Fig. 6. \mathbf{M} is a *permutation matrix* if the number of nodes in two graphs are equal. A *slack* row and column are added to \mathbf{M} to represent missing/extra nodes. We refer to the nodes by G_a and \bar{G}_i , and the links by G_{ab} and \bar{G}_{ij} , respectively, where $a, b = 1, \dots, A$, and $i, j = 1, \dots, I$, i.e.,

$$\mathbf{M}_{ai} = \begin{cases} 1 & \text{if the node } a \in G \text{ corresponds to node } i \in \bar{G} \\ 0 & \text{otherwise.} \end{cases}$$

An objective *energy function* $E(\mathbf{M})$ is defined for each possible assignment \mathbf{M} . For a *quadratic* matching problem:

$$E(\mathbf{M}) = \sum_{i=1}^I \sum_{a=1}^A \sum_{b=1}^A \sum_{j=1}^I \mathbf{M}_{ai} \mathbf{M}_{bj} L_{aibj}, \quad (3)$$

where L_{aibj} represents the *compatibility* between links G_{ab} and \bar{G}_{ij} . Maximizing E yields the best matching between G and \bar{G} . A significant idea in [32] is to extend the above discrete assignment problem to a *continuous* one by embedding it into a large space, where *gradient descent* can be performed to iteratively move from one assignment to another. In this context, the continuous matching matrix \mathbf{M} takes values between 0 and 1, satisfying the constraint of being a *doubly stochastic* matrix: $\sum_a \mathbf{M}_{ai} = 1$ and $\sum_i \mathbf{M}_{ai} = 1$ [62]. The \mathcal{GA} algorithm then *differentially* moves from one assignment \mathbf{M} to another, guided by refining the matching energy $E(\mathbf{M})$ in a *graduated non-convexity* setting [32], which slowly modifies \mathbf{M} towards a 0 or 1 discretization. The Taylor expansion of E is:

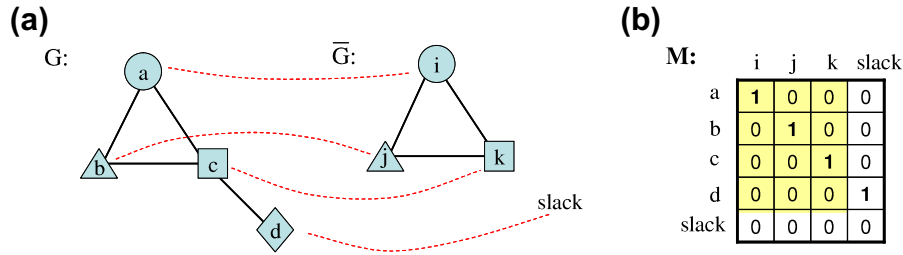


Fig. 6. (a) The matching of two synthetic graphs G and \bar{G} , where the extra node is matched into the *slack* column of \mathbf{M} .

$$E(\mathbf{M}) = E(\mathbf{M}^0) + \sum_{a=1}^A \sum_{i=1}^I Q_{ai} (\mathbf{M}_{ai} - \mathbf{M}_{ai}^0), \quad (4)$$

where the derivative matrix Q is:

$$Q = \frac{\partial E}{\partial \mathbf{M}_{ai}} \Big|_{\mathbf{M}=\mathbf{M}^0} = \sum_{b=1}^A \sum_{j=1}^I \mathbf{M}_{bj}^0 L_{ajib}. \quad (5)$$

The problem of maximizing E is then turned into maximizing $\sum_{a=1}^A \sum_{i=1}^I Q_{ai} \mathbf{M}_{ai}$, which is (again) an *assignment problem* [32] solvable by *softassign*. The $\mathcal{G}\mathcal{A}$ algorithm iteratively (and gradually) modifies an initial \mathbf{M} toward discretization by decreasing a parameter T ('temperature' in annealing), which controls the convexity of the energy landscape to avoid poor local minima. In each iteration, the matching matrix \mathbf{M} is best estimated and normalized toward a final assignment, ensuring it remains the continuous analogue of a discrete assignment, using a technique discovered by Sinkhorn [62].

Our implementation of the $\mathcal{G}\mathcal{A}$ algorithm follows three nested iterations summarized in Fig. 7. The algorithm starts with an initial \mathbf{M} of an unbiased equal assignment. In each step in iteration A with a current temperature T and assignment \mathbf{M} , the derivative $Q(\mathbf{M})$ is estimated by optimizing the compatibility measures (1 for a perfect match, 0 for no match) between the graph nodes and links using the current assignment \mathbf{M} . The sub-iterations B and C update \mathbf{M} through *softassign*, where the rows and columns of \mathbf{M} are repeatedly normalized and converge into a doubly stochastic matrix. This procedure is repeated by decreasing T until the assignment \mathbf{M} converges or a sufficient number of iterations are reached.

Begin A: (Do A until $T < T_f$ or # *iters.* $> I_A$)

Begin B: (until \mathbf{M} converges or # *iters.* $> I_B$)

$$Q_{ai} \leftarrow - \frac{\partial E}{\partial \mathbf{M}_{ai}} \text{ estimated from graph compatibilities.}$$

$$\mathbf{M}_{ai}^0 \leftarrow \exp(1/T \cdot Q_{ai})$$

Begin C: (until $\hat{\mathbf{M}}$ converges or # *iters.* $> I_C$)

Update $\hat{\mathbf{M}}$ by normalizing across all rows:

$$\hat{\mathbf{M}}_{ai}^1 \leftarrow \frac{\mathbf{M}_{ai}^0}{\sum_{i=1}^{I+1} \mathbf{M}_{ai}^0}$$

Update $\hat{\mathbf{M}}$ by normalizing across all columns:

$$\hat{\mathbf{M}}_{ai}^0 \leftarrow \frac{\hat{\mathbf{M}}_{ai}^1}{\sum_{a=1}^{A+1} \hat{\mathbf{M}}_{ai}^1}$$

End C

End B

$$T \leftarrow T_r \cdot T$$

End A

Fig. 7. (Left, adapted from [32]) A summary of the graduated assignment algorithm in [32]. (Right) The $\mathcal{G}\mathcal{A}$ parameters with our suggested values.

4.2. Extending $\mathcal{G}\mathcal{A}$ to match $\mathcal{M}\mathcal{S}$ hypergraphs

The original $\mathcal{G}\mathcal{A}$ is shown to be successful in matching two *attributed relational graphs* by combining the energies of node-to-node assignments (1st-order term) with link-to-link assignments (2nd-order term) [32]. In our case to match the hypergraphs with yet another dimension, we introduce a 3rd-order assignment to match the medial sheets (hyperlinks) of the $\mathcal{M}\mathcal{S}$ hypergraph [16]. While the medial sheets could contain complex topology in general, we indirectly match them by matching individual *corners* of the sheet (where medial curves intersect), whose overall effects accumulate to match the sheets.

In defining the energy E to match the $\mathcal{M}\mathcal{S}$ hypergraphs, ideally E should reflect the true similarity between two shapes. However it is difficult to model the exact shape variations in practice. Instead, we make E reflect the *component-wise* compatibility between two hypergraphs $\mathcal{M}\mathcal{S}$ and $\bar{\mathcal{M}}\mathcal{S}$, which composes of two measures, each reflects the *structural* and the *parametric* variations in matching the skeletal graph structures. We then optimize the overall similarity by summing up all compatibility measures (Section 5).

We further exploit two thoughts in formulating a proper distance metric to compare the similarity/dissimilarity in the $\mathcal{M}\mathcal{S}$ hypergraph matching. First, given two non-negative measures m_1 and m_2 extracted from two shapes S_1 and S_2 that could be without normalization, the question is how to estimate a normalized similarity measure that is between 0 and 1. We propose to normalize the measures m_i w.r.t. the maximum value in shape S_i and then compare them using a *square-root distance* $d^s = \sqrt{|m_1 - m_2|}$. This is motivated by three reasons [56]: (a) a re-interpretation of Weber's law [68], (b) to maintain sensitivity to variations when

| Parameter | Description |
|------------------------|--|
| $T_0 = 100$ | The initial temperature |
| $T_f = 0.01$ | The termination temperature |
| $T_r = 0.95$ | Rate in decreasing temperature |
| $I_A = 100$ | Maximum iterations in <i>softassign</i> |
| $I_B = 4$ | Maximum iterations in loop B |
| $I_C = 30$ | Maximum iterations in loop C |
| $\epsilon_B = 0.005$ | Criterion of convergence of \mathbf{M} |
| $\epsilon_C = 0.0005$ | Criterion of convergence of $\hat{\mathbf{M}}$ |
| $\epsilon_S = 0.00005$ | Criterion of convergence in <i>softassign</i> |

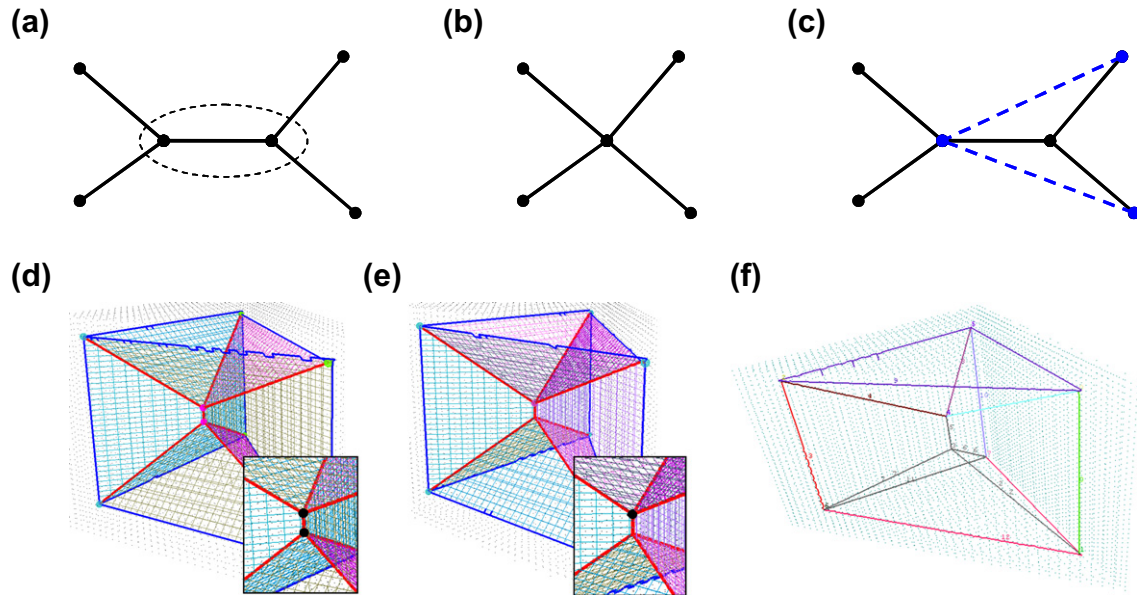


Fig. 8. The adding of virtual links correlates a *contracting* edit of (a–c) a graph link in 2D and (d and e) a curve of a hypergraph in 3D. (f) Shows the matching of two \mathcal{MS} hypergraphs across a *contract transform* [15], where the mismatch links are shown in gray.

two items are close, and (c) to reduce sensitivity when two items are very distant. We found this norm to perform better for our application than others, e.g., the weighted distance $\left(\frac{m_1 - m_2}{\max(m_1, m_2)}\right)$, the logarithm of distance, and other metrics [56].³ Second, a set of *virtual links* [56] (in addition to the medial curves/links) is introduced which improves the matching robustness in tolerating structural differences (detailed below).

Our \mathcal{MS} matching algorithm is described as follows. We first regularize the \mathcal{MS} by applying a set of transforms [15] to simplify it across generic transitions, which bring the two hypergraphs close in structure, such that the graph matching scheme is manageable to yield correct correspondence. The remaining difference is then matched to evaluate similarity. Since the \mathcal{GA} handles missing and extra nodes (by the slack variables), we can enforce the matching across structural differences by “simulating” them across remaining transitions, e.g., by connecting the nodes that will be brought together in the future transitions by adding *virtual links*, Fig. 8, which simulates the effect of applying further \mathcal{MS} transforms [14]. We only add virtual links to the configurations that warrant high possibility of transitions (with slight shape variations). This helps to explore the better but difficult-to-compute *edit-distance* [55] in the candidate spaces to improve the matching as well as its robustness. It essentially complements the one-to-one assignment nature of the \mathcal{GA} graph-matching scheme in handling structural variations.⁴ The use of virtual links also provides a way to match the \mathcal{MS} hypergraph robustly across transitions near a high-order \mathcal{MS} node. To illustrate, Fig. 8 shows an example of

robustly matching an A_1^5 node to a set of two A_1^3 nodes near an A_1^5 *contract transform* of the \mathcal{MS} [15].

5. Matching the \mathcal{MS} hypergraphs: componentwise compatibility measures

This section describes our component-wise node-to-node, curve-to-curve, and sheet-to-sheet compatibility measures in matching two hypergraphs \mathcal{MS} and $\overline{\mathcal{MS}}$. We assume the scaffolds have been properly regularized and we follow the matching framework described in the previous section. The goal is to define compatibility measures for all assignments \mathbf{M} , such that the \mathcal{GA} can migrate through the space to produce a final correspondence. Again the similarity between \mathcal{MS} hypergraphs could be measured qualitatively, or **structurally**, e.g. whether a link/hyperlink exists or whether their types are consistent or not. They also could be measured more quantitatively, in a **parametric** way, i.e. by delicately comparing the attributes along the medial curves/sheets to define a metric.

Consider that a shape can deform via a sequence of (canonical) transformations, dissimilarity between shapes is the amount of *minimum* changes in the space of transformations. We briefly consider the following measures in estimating the dissimilarity during shape deformations: (a) *stretching* or *compressing*: the similarity is translated into the length comparison of medial curves; (b) *fattening* or *thinning*: the similarity is measured by the shock acceleration functions; (c) *bending* which affects the curvature along the \mathcal{MA} . These terms are measured in all hypergraph components (namely, all pairs of nodes, curves, and sheets) in order to compute the compatibility estimate.

Table 1 overviews the main compatibility terms in measuring the shape similarity via matching their skeletal graphs. This is the main content of this paper, which we shall explain in detail in the following sections.

5.1. The first-order node compatibility (\mathcal{N})

Two shock nodes $N_a \in \mathcal{MS}$ and $\overline{N}_i \in \overline{\mathcal{MS}}$ are compared **structurally** on their node types and incident shock curve types.

³ To further illustrate the efficacy of the square-root distance d^s , consider the comparison of two \mathcal{MS} curves of a single shape in matching to itself, i.e., in the compatibility matrix of size $n \times n$ (Fig. 9c), where n is the number of \mathcal{MS} curves. The diagonal elements should have dissimilarity (distance) 0 and all other should have arbitrary large values. Note that these large values as results of the curve matching edit-distance (d_{ed}) and Euclidean distance (d_{eu}) are not normalized and could be arbitrarily large, depending on the length of the curve and the local shape radius, etc. One could take the logarithm of such values to avoid improper scaling, however the log maps 0 to ∞ . We found that the square-root distance after normalization by each shape’s maximum value is more suitable and works the best in practice.

⁴ We can simply use the procedure for the *detection* of transforms detailed in [15] to look for such candidate positions to add virtual links (by allowing a larger transform cost threshold).

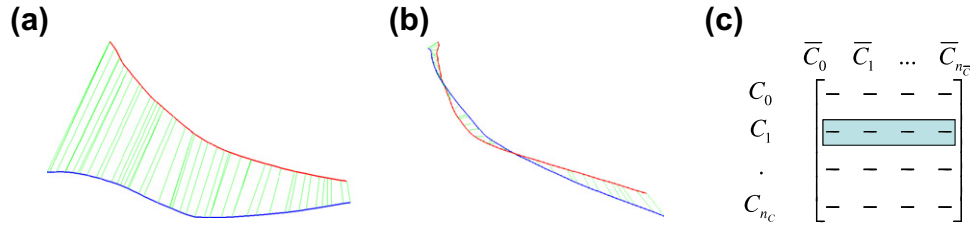


Fig. 9. (a) The D.P. matching of two shock curves by considering their geometry as 3D space curves together with other shock attributes. (b) The rigid alignment by using the D.P. correspondence to compute the optimal Euclidean distance between them. (c) Result stored in the D.P. result table, and the normalization of the compatibility is against the row (see text).

Table 1
Compatibility terms used in matching \mathcal{MS} hypergraphs.

| | Structural similarity | Parametric similarity |
|----------------|---|---|
| Node | Node type, incident curve types | Radius r , ∇r along incident curves, angle of curves at sheet corners |
| Curve (link) | Existence, curve type, ending node types, orientation | $\sum r_i$, edit-distance (elastic deformations), Euclidean distance |
| Sheet (corner) | Existence, incident curve types, corner node type | Corner angle, radius r , ∇r at the corner, $\sum r_i$ (to approximate volume) |

Table 2
Difference $d[\cdot, \cdot]$ between the *general* and *high-order* \mathcal{MS} nodes used to measure their structural compatibility.

| | A_1A_3 | A_1^4 | $A_1^2A_3$ | A_1^5 | $A_1^3A_3$ | A_1^6 | $A_1^4A_3$ | A_1^7 | $A_1^5A_3$ | A_1^8 | ... | $A_1^m A_3$ | A_1^n |
|-------------|----------|---------|------------|---------|------------|---------|------------|---------|------------|---------|-----|-------------------|-----------------|
| A_1A_3 | 0 | 3/4 | 1/5 | 4/5 | 2/6 | 5/6 | 3/7 | 6/7 | 4/8 | 7/8 | ... | $\frac{m-1}{m+3}$ | $\frac{n-1}{n}$ |
| A_1^4 | | 0 | 3/5 | 1/5 | 3/6 | 2/6 | 3/7 | 3/7 | 4/8 | 4/8 | ... | $\frac{m-1}{m+3}$ | $\frac{n-4}{n}$ |
| $A_1^2A_3$ | | | 0 | 3/5 | 1/6 | 4/6 | 2/7 | 5/7 | 3/8 | 6/8 | ... | $\frac{m-2}{m+3}$ | $\frac{n-2}{n}$ |
| A_1^5 | | | | 0 | 3/6 | 1/6 | 3/7 | 2/7 | 3/8 | 3/8 | ... | $\frac{m-2}{m+3}$ | $\frac{n-5}{n}$ |
| $A_1^3A_3$ | | | | | 0 | 3/6 | 1/7 | 4/7 | 2/8 | 5/8 | ... | $\frac{m-3}{m+3}$ | $\frac{n-3}{n}$ |
| A_1^6 | | | | | | 0 | 3/7 | 1/7 | 3/8 | 2/8 | ... | $\frac{m-3}{m+3}$ | $\frac{n-6}{n}$ |
| $A_1^4A_3$ | | | | | | | 0 | 3/7 | 1/8 | 4/8 | ... | $\frac{m-4}{m+3}$ | $\frac{n-4}{n}$ |
| A_1^7 | | | | | | | | 0 | 3/8 | 1/8 | ... | $\frac{m-4}{m+3}$ | $\frac{n-7}{n}$ |
| $A_1^5A_3$ | | | | | | | | | 0 | 3/8 | ... | $\frac{m-5}{m+3}$ | $\frac{n-5}{n}$ |
| A_1^8 | | | | | | | | | | 0 | ... | $\frac{m-5}{m+3}$ | $\frac{n-8}{n}$ |
| ... | | | | | | | | | | | 0 | ... | ... |
| $A_1^m A_3$ | | | | | | | | | | | | 0 | ... |
| A_1^n | | | | | | | | | | | | | 0 |

We observe two sets of shock nodes: one from the classification of the 5 generic \mathcal{MA} nodes (namely, $A_1^2, A_1^3, A_3, A_1^4, A_1A_3$) in [30] and the other of *high-order* nodes produced by applying \mathcal{MS} transforms in the regularization process [15]. The above two sets can be re-organized into two categories [14], namely

$$A_1^m A_3 \text{ and } A_1^n, \text{ where } m, \bar{m} \geq 1 \text{ and } n, \bar{n} \geq 4.$$

We propose to compare the \mathcal{MS} nodes intrinsically, in other words, by comparing their structural compatibility including the shock node types, incident shock curve types, etc. and penalizing the differences. For example, an intuitive idea is to avoid matching an interior A_1^4 node to an A_1A_3 node near the shape boundary. We penalize the difference of shock node types by their difference in their *shock contact order*, and normalize it (to be within 0 and 1) by the maximum shock singularity between the two, (e.g., mimicking a weighted distance). To illustrate, we define a unit difference of an A_1 to be 1, and the difference of an A_3 to be 3 (three units); so the difference between an A_1A_3 and A_1^4 nodes are three normalized by a total contact order of four, leading to 3/4. This rule can be generalized to compare all high-order \mathcal{MS} nodes $A_1^m A_3$ and A_1^n as discussed in [14]. The result is summarized as follows:

$$d[A_1^m A_3, A_1^n] = \frac{\max(n-m, 3)}{\max(n, m+3)}, d[A_1^m, A_1^n] = \frac{|n-\bar{n}|}{\max(n, \bar{n})}, \tag{6}$$

$$d[A_1^m A_3, A_1^{\bar{m}} A_3] = \frac{|m-\bar{m}|}{\max(m, \bar{m})+3},$$

where $d[\cdot, \cdot]$ denotes the *node type difference*. Table 2 lists the values of d between a few high-order \mathcal{MS} nodes frequently observed in practice.⁵

The structural node compatibility \mathcal{N}_s is defined as the complement of node type difference,

$$\mathcal{N}_s[N_a, \bar{N}_i] = 1 - d^s[N_a, \bar{N}_i], \tag{7}$$

such that $\mathcal{N}_s = 1$ if the shock types are identical, and $\mathcal{N}_s = 0$ if the shock types have nothing in common. $d^s = \sqrt{d}$.

We consider three main terms between two shock nodes in the **parametric** compatibility measure: (i) difference of the shock node *radius* r . (ii) difference of the *gradient* of radius (∇r) along their incident shock curves. Since there exist numerous incident curves at a

⁵ In [14], we have also discussed the special shock nodes such as the *corner shock node* N_{cor} (intersection of one A_1^3 axial and three A_3 curves) and the *double-fin node* (A_1A_3)₂ and the *triple-fin node* (A_1A_3)₃. The distance between them is defined similarly.

shock node (for example, there are four curves at an A_1^4 node), we simply take the maximum and minimum measures (∇r^+ , ∇r^-) to compute the difference.⁶ (iii) the *angles* a of the incident sheet corner between a pair of shock curves. Again there exists numerous sheet corners at each node (for example, there are six sheets intersecting at an A_1^4 node), we only take the maximum and minimum measures (a^+ , a^-). The parametric node compatibility \mathcal{N}_p is then:

$$\begin{aligned} \mathcal{N}_p[N_a, \bar{N}_i] = & 1 - w_r^n \cdot d^s[r(N_a), r(\bar{N}_i)] \\ & - \frac{w_g^n}{2} d^s[\nabla r^+(N_a), \nabla r^+(\bar{N}_i)] \\ & - \frac{w_g^n}{2} d^s[\nabla r^-(N_a), \nabla r^-(\bar{N}_i)] - \frac{w_a^n}{2} d^s[a^+(N_a), a^+(\bar{N}_i)] \\ & - \frac{w_a^n}{2} d^s[a^-(N_a), a^-(\bar{N}_i)]. \end{aligned} \quad (8)$$

where the weighting constants $w_r^n = 0.5$, $w_g^n = 0.25$, $w_a^n = 0.25$ specify the relative importance between different measures obtained from their respective hypergraph components. They could be interpreted as confidence measures—to what extent one should trust these measures in accessing an overall similarity.

Finally, the 1st-order node compatibility for hypergraph matching is:

$$\mathcal{N}_{ai}[N_a, \bar{N}_i] = \mathcal{N}_s \cdot \mathcal{N}_p. \quad (9)$$

Note that the node compatibility measure is purely local. It only depends on the local shape corresponding to the maximum circumscribing sphere of the \mathcal{M}_A .

5.2. The second-order curve compatibility (\mathcal{L})

Two shock curves $C_{ab} \in \mathcal{MS}$ and $\bar{C}_{ij} \in \overline{\mathcal{MS}}$ can be compared **structurally** over their local curve types, curve orientations, and ending node types. We look for compatibility measures to reflect the following *three* aspects in matching two medial curves $C_{ab} \in \mathcal{MS}$ and $\bar{C}_{ij} \in \overline{\mathcal{MS}}$: (i) the existence of the shock curve (to avoid the case if any of the shock curves C_{ab} or \bar{C}_{ij} does not exist), (ii) the shock curve type (to avoid the matching of an A_3 curve to an A_1^3 curve), and (iii) the two shock end node types, which also considers the *orientation* of the shock curves into the matching, namely, if $\mathcal{N}_s[N_a, \bar{N}_i]$ or $\mathcal{N}_s[N_b, \bar{N}_j]$ is low, $\mathcal{L}_s[C_{ab}, \bar{C}_{ij}]$ should be low.

We define the structural curve (link) compatibility (\mathcal{L}_s) as follows. If C_{ab} or \bar{C}_{ij} is missing or the curve types are different, $\mathcal{L}_s[C_{ab}, \bar{C}_{ij}] = 0$; otherwise,

$$\mathcal{L}_s = 1 - w_n^c \cdot d^s[N_a, \bar{N}_i] - w_n^c \cdot d^s[N_b, \bar{N}_j], \quad (10)$$

where the weighting parameter $w_n^c = 0.2$ penalizes the difference between the ending shock node types.

We consider three main terms in the **parametric** compatibility measure between C_{ab} and \bar{C}_{ij} : (i) *integration of shock radius* along the curves to reflect corresponding shape volume,

$$V(C) = \int_{s \in C} r \cdot ds \approx \sum_{k=1}^{n_{\text{sample}}} r(C_k), \quad (11)$$

with a normalization done by dividing by a maximum value in \mathcal{MS} and $\overline{\mathcal{MS}}$, such that $0 \leq V^n(C_{ab}), V^n(\bar{C}_{ij}) \leq 1$. (ii) *edit-distance* $d_{ed}[C_{ab}, \bar{C}_{ij}]$ optimizing the *elastic* deformation between the two curves to obtain an optimal alignment minimizing the following energy terms via *dynamic programming* (D.P.) [54,55]: (a) *stretching* difference $ds(C_p, C_{p-1}, \bar{C}_q, \bar{C}_{q-1})$, where p, q are indices of the fine-scale mesh vertices along the curves, (b) *bending* difference dt , (c)

shock *radius* difference dr , and (d) the *angle* difference da between incident sheets, Fig. 9a. Specifically, two shock curves are matched both as space curves (in their elastic bending and stretching terms) and as a joined skeleton-boundary matching to approximate their similarity.⁷

$$\min \{[ds + dr] + w_a^l \cdot [dt + da]\}, \quad (12)$$

where the weighting constant $w_a^l = 0.1$ specifies the ratio between the *length* and *angle* measures (the value is relative to the *scale* of shapes as in [55]). (iii) an optional *Euclidean distance* d_{Eu} available from the correspondence of the above edit-distance matching, Fig. 9b. Specifically, we compute the optimal rotation and translation (R, T) to align C_{ab} to \bar{C}_{ij} , and compute the average distance between the corresponding pairs, Fig. 9b. This term enhances the matching of *rigid* objects or shapes with slight deformations. It should be avoided for matching *deformable* objects or shapes across large variations. The parametric curve compatibility is then:

$$\begin{aligned} \mathcal{L}_p[C_{ab}, \bar{C}_{ij}] = & 1 - w_d^l \cdot d_{ed}^s[C_{ab}, \bar{C}_{ij}] - w_e^l \cdot d_{Eu}^s[C_{ab}, \bar{C}_{ij}] - w_v^l \\ & \cdot d^s[V(C_{ab}), V(\bar{C}_{ij})], \end{aligned} \quad (13)$$

where d_{ed}^s and d_{Eu}^s are the square-root of d_{ed} and d_{Eu} after normalization by respective maximum values. The weighting constants are suggested as $w_d^l = 0.33$, $w_e^l = 0.33$, and $w_v^l = 0.34$ to specify the influence between these measurements.

Finally, the 2nd-order link (curve) compatibility for hypergraph matching is:

$$\mathcal{L}_{aibj}[C_{ab}, \bar{C}_{ij}] = \mathcal{L}_s \cdot \mathcal{L}_p. \quad (14)$$

We observed in practice the curve compatibility measure provides a strong cue in discriminating shape variations.

5.3. The third-order sheet (corner) compatibility (\mathcal{C})

Two shock sheet corners $S_{abc} \in \mathcal{MS}$ and $\bar{S}_{ijk} \in \overline{\mathcal{MS}}$ are compared **structurally** on their boundary shock *curve type* and the shock *node types* at the corner. Specifically, if S_{abc} or \bar{S}_{ijk} is missing or (C_{ab}, \bar{C}_{ij}) or (C_{bc}, \bar{C}_{jk}) are of different types, $\mathcal{C}_s = 0$; otherwise,

$$\begin{aligned} \mathcal{C}_s(S_{abc}, \bar{S}_{ijk}) = & 1 - w_{n1}^c d^s[N_b, \bar{N}_j] - w_{n2}^c d^s[N_a, \bar{N}_i] \\ & - w_{n2}^c d^s[N_c, \bar{N}_k] \end{aligned} \quad (15)$$

with weighting constants are chosen as $w_{n1}^c = 0.8$ and $w_{n2}^c = 0.1$. We make $w_{n1}^c + 2w_{n2}^c = 1$ to completely determine the structural compatibility, due to the fact that there is no structural information from the medial sheets (all of A_2^2 type).

We consider four main terms in the **parametric** compatibility measure: (i) shock radius r of the corner node (N_b and \bar{N}_j), which can be approximated by the average of the radius gradients along the two incident curves of each corner, i.e., (C_{ba}, \bar{C}_{bc}) and $(\bar{C}_{ji}, \bar{C}_{jk})$ that can be computed similarly as in Section 5.1. (ii) gradient of shock radius (∇r) along the sheet (bisector curve at the corner), (iii) corner angle between $\angle(S_{abc})$ and $\angle(\bar{S}_{ijk})$, (iv) corresponding shape volume V of the sheet (integration of shock radius). This can be approximated by summing up the radius of all sheet elements: $V(S) = \int_{s \in S} r \cdot ds \approx \sum_{k=1}^{n_{\text{sample}}} r(S_k)$.

The parametric sheet (corner) compatibility \mathcal{C}_p is defined as:

$$\begin{aligned} \mathcal{C}_p(S_{abc}, \bar{S}_{ijk}) = & 1 - w_r^c d^s[r(N_b), r(\bar{N}_j)] - w_g^c d^s[\nabla r(S), \nabla r(\bar{S})] \\ & - w_a^c d^s[\angle(S_{abc}), \angle(\bar{S}_{ijk})] - w_v^c d^s[V(S), V(\bar{S})]. \end{aligned} \quad (16)$$

⁷ We use an *alignment curve* α to represent the result of the correspondence between C_{ab} and \bar{C}_{ij} [55,54]. We follow standard finite difference approach to compute the following differential terms of the shock curves as 3D space curves: stretching and derivatives ϕ , ϕ_s , ϕ_{ss} , bending and derivatives θ , θ_s , θ_{ss} , tangent T , normal N , binormal B , curvature κ , and torsion τ .

⁶ Two additional reasons motivate this design: (a) the measures in between the maximum and minimum are less salient and less robust to compare; and (b) the A_1A_3 node has only two incident curves, thus selecting two distinct curves is most general.

| | | | | | | |
|----------------------|--|--|--|--|--|--|
| | | | | | | |
| N: 80, C: 105, S: 26 | | | | | | |
| N: 40, C: 56, S: 17 | | | | | | |
| N: 35, C: 54, S: 20 | | | | | | |
| N: 8, C: 10, S: 3 | | | | | | |
| N: 12, C: 18, S: 7 | | | | | | |
| N: 19, C: 26, S: 8 | | | | | | |

Fig. 10. Result of matching the \mathcal{MS} hypergraphs of the (hamate) carpal bones across six patients [47]. Number of medial nodes (N), curves (C), and sheets (S) of the \mathcal{MS} 's after regularization are labeled on the left. We use the node correspondence to compute a rigid transformation to align the bones for visualization. Closely aligned bones are manually marked with 'green o' (16 ones), while roughly aligned ones are marked with 'blue -' (10 ones) and misaligned cases are marked with 'red x' (4 ones), out of a visual examination. Since visual misalignment does not necessarily indicate a wrong match, this experiment only evaluates qualitatively how the method performs on matching similar shapes with large skeletal structure variations. (For interpretation of the references to colour in this figure legend, the reader is referred to the web version of this article.)

where the weighting parameters $w_r^c = 0.2$, $w_g^c = 0.3$, $w_a^c = 0.3$, and $w_v^c = 0.2$ to balance between different measurements.

Finally, the third-order sheet (corner) compatibility is:

$$\mathcal{C}_{aibjck}[S_{abc}, \bar{S}_{ijk}] = C_s \cdot C_p. \quad (17)$$

6. Computing the post-matching similarity

In this section, we derive a *global* similarity measure as an energy functional using the matching result, *i.e.*, the final assignment matrix \mathbf{M} and the compatibilities defined in Section 5. The energy $E(\mathbf{M})$ between two hypergraphs \mathcal{MS} and $\bar{\mathcal{MS}}$ is defined as:

$$E[\mathcal{MS}, \bar{\mathcal{MS}}, \mathbf{M}] = w^N \cdot E_N + w^L \cdot E_L + w^C \cdot E_C. \quad (18)$$

where $w^N = 0.3$, $w^L = 0.5$, $w^C = 0.4$ are the weighting constants between the node (E_N), curve (E_L), and sheet corner (E_C) energies:

$$E_N = \sum_{a=1}^A \sum_{i=1}^I \mathbf{M}_{ai} \mathcal{N}_{ai}[N_a, \bar{N}_i],$$

$$E_L = \sum_{a=1}^A \sum_{i=1}^I \sum_{b=1}^A \sum_{j=1}^I \mathbf{M}_{ai} \mathbf{M}_{bj} \mathcal{L}_{aibj}[C_{ab}, \bar{C}_{ij}], \quad (19)$$

$$E_C = \sum_{a=1}^A \sum_{i=1}^I \sum_{b=1}^A \sum_{j=1}^I \sum_{c=1}^A \sum_{k=1}^I \mathbf{M}_{ai} \mathbf{M}_{bj} \mathbf{M}_{ck} \mathcal{C}_{aibjck}[S_{abc}, \bar{S}_{ijk}].$$

The weighted sum of the compatibility measure allows us to decompose the non-trivial task of matching the whole medial hypergraph structure into matching its sub-components. The weights are selected based on practical observation on how well each component matches and discriminates shapes in general.

Our initial implementation of Eq. 18 reveals that the energy defined in this way varies with the number of nodes and links in each hypergraph, thus the similarity between pairs of shapes could not be universally compared. This motivates a normalization of each component of the energy functional by the maximum possible value for each case [56]. The *normalized similarity energy* E^n is defined as:

| | | | | | | | | | | | | | | | | | | | | |
|---|---|---|---|---|---|---|---|---|---|---|--|---|---|---|---|---|---|---|---|--------------|
|  |  |  |  |  |  |  |  |  |  |  |  |  |  |  |  |  |  |  |  | |
|  | 1.000 | 0.870 | 0.710 | 0.692 | 0.638 | 0.535 | 0.539 | 0.530 | 0.479 | 0.523 | 0.223 | 0.202 | 0.251 | 0.282 | 0.385 | 0.336 | 0.237 | 0.163 | 0.076 | 0.162 |
|  | 0.790 | 1.000 | 0.700 | 0.660 | 0.647 | 0.545 | 0.559 | 0.529 | 0.519 | 0.547 | 0.202 | 0.206 | 0.208 | 0.279 | 0.460 | 0.363 | 0.238 | 0.234 | 0.098 | 0.219 |
|  | 0.701 | 0.660 | 1.000 | 0.869 | 0.955 | 0.612 | 0.553 | 0.598 | 0.555 | 0.600 | 0.238 | 0.082 | 0.256 | 0.279 | 0.444 | 0.350 | 0.250 | 0.217 | 0.082 | 0.171 |
|  | 0.719 | 0.699 | 0.843 | 1.000 | 0.877 | 0.484 | 0.475 | 0.478 | 0.589 | 0.531 | 0.223 | 0.225 | 0.230 | 0.264 | 0.348 | 0.422 | 0.223 | 0.188 | 0.106 | 0.154 |
|  | 0.646 | 0.661 | 0.953 | 0.893 | 1.000 | 0.591 | 0.604 | 0.608 | 0.565 | 0.594 | 0.243 | 0.138 | 0.250 | 0.275 | 0.421 | 0.365 | 0.292 | 0.197 | 0.103 | 0.150 |
|  | 0.578 | 0.577 | 0.615 | 0.671 | 0.646 | 1.000 | 0.917 | 0.934 | 0.862 | 0.730 | 0.148 | 0.108 | 0.140 | 0.265 | 0.247 | 0.244 | 0.271 | 0.147 | 0.010 | 0.119 |
|  | 0.583 | 0.577 | 0.624 | 0.689 | 0.657 | 0.908 | 1.000 | 0.924 | 0.899 | 0.823 | 0.138 | 0.199 | 0.180 | 0.238 | 0.263 | 0.262 | 0.268 | 0.147 | 0.017 | 0.119 |
|  | 0.575 | 0.562 | 0.619 | 0.681 | 0.645 | 0.925 | 0.918 | 1.000 | 0.885 | 0.729 | 0.146 | 0.178 | 0.153 | 0.238 | 0.256 | 0.251 | 0.275 | 0.141 | 0.009 | 0.117 |
|  | 0.556 | 0.538 | 0.594 | 0.673 | 0.610 | 0.867 | 0.907 | 0.896 | 1.000 | 0.854 | 0.337 | 0.200 | 0.300 | 0.351 | 0.343 | 0.362 | 0.312 | 0.176 | 0.097 | 0.183 |
|  | 0.585 | 0.597 | 0.645 | 0.668 | 0.659 | 0.734 | 0.832 | 0.733 | 0.818 | 1.000 | 0.311 | 0.261 | 0.290 | 0.324 | 0.404 | 0.383 | 0.329 | 0.260 | 0.083 | 0.176 |
|  | 0.157 | 0.131 | 0.169 | 0.165 | 0.172 | 0.133 | 0.140 | 0.132 | 0.327 | 0.267 | 1.000 | 0.613 | 0.903 | 0.505 | 0.220 | 0.311 | 0.190 | 0.012 | 0.005 | 0.041 |
|  | 0.209 | 0.562 | 0.085 | 0.187 | 0.136 | 0.277 | 0.287 | 0.279 | 0.160 | 0.340 | 0.662 | 1.000 | 0.597 | 0.496 | 0.179 | 0.282 | 0.143 | 0.038 | 0.007 | 0.061 |
|  | 0.159 | 0.173 | 0.188 | 0.192 | 0.181 | 0.146 | 0.142 | 0.138 | 0.334 | 0.232 | 0.931 | 0.596 | 1.000 | 0.527 | 0.208 | 0.338 | 0.167 | 0.013 | 0.011 | 0.040 |
|  | 0.278 | 0.246 | 0.266 | 0.277 | 0.274 | 0.278 | 0.303 | 0.319 | 0.370 | 0.299 | 0.492 | 0.192 | 0.493 | 1.000 | 0.236 | 0.292 | 0.203 | 0.036 | 0.022 | 0.121 |
|  | 0.427 | 0.444 | 0.420 | 0.392 | 0.360 | 0.243 | 0.263 | 0.234 | 0.292 | 0.328 | 0.204 | 0.016 | 0.205 | 0.218 | 1.000 | 0.483 | 0.458 | 0.118 | 0.033 | 0.145 |
|  | 0.399 | 0.413 | 0.245 | 0.437 | 0.235 | 0.306 | 0.306 | 0.304 | 0.370 | 0.370 | 0.423 | 0.283 | 0.401 | 0.226 | 0.513 | 1.000 | 0.493 | 0.125 | 0.048 | 0.170 |
|  | 0.277 | 0.220 | 0.341 | 0.223 | 0.331 | 0.241 | 0.281 | 0.219 | 0.296 | 0.382 | 0.182 | 0.138 | 0.173 | 0.191 | 0.528 | 0.493 | 1.000 | 0.018 | 0.012 | 0.055 |
|  | 0.191 | 0.194 | 0.196 | 0.183 | 0.182 | 0.065 | 0.130 | 0.127 | 0.142 | 0.231 | 0.016 | 0.046 | 0.016 | 0.052 | 0.100 | 0.123 | 0.033 | 1.000 | 0.287 | 0.311 |
|  | 0.093 | 0.046 | 0.087 | 0.102 | 0.099 | 0.008 | 0.011 | 0.023 | 0.019 | 0.034 | 0.008 | 0.012 | 0.021 | 0.017 | 0.032 | 0.050 | 0.015 | 0.274 | 1.000 | 0.239 |
|  | 0.016 | 0.017 | 0.015 | 0.017 | 0.015 | 0.012 | 0.013 | 0.015 | 0.013 | 0.014 | 0.011 | 0.012 | 0.011 | 0.012 | 0.114 | 0.137 | 0.079 | 0.217 | 0.258 | 1.000 |

Fig. 11. Similarity metric computed for a small shape database. Correct matches are highlighted in boldface in **black** (same object) and **blue**, while erroneous ones are in red. Observe that the *within-category* similarity is well-preserved and distinct from non-category shapes. (For interpretation of the references to colour in this figure legend, the reader is referred to the web version of this article.)

$$\begin{aligned}
 E^n[\mathcal{MS}, \overline{\mathcal{MS}}, \mathbf{M}] &= w^N \sum_{a=1}^A \sum_{i=1}^I \frac{\mathbf{M}_{ai} \mathcal{N}_{ai}}{\mathbf{M}_{ai}} + w^L \sum_{a=1}^A \sum_{i=1}^I \sum_{b=1}^A \sum_{j=1}^I \\
 &\times \frac{\mathbf{M}_{ai} \mathbf{M}_{bj} \mathcal{L}_{aibj}}{\mathbf{M}_{ai} \mathbf{M}_{bj} \mathcal{L}_{aibj}^{\max}} + w^C \sum_{a=1}^A \sum_{i=1}^I \sum_{b=1}^A \sum_{j=1}^I \sum_{c=1}^A \\
 &\times \sum_{k=1}^I \frac{\mathbf{M}_{ai} \mathbf{M}_{bj} \cdot \mathbf{M}_{ck} \mathcal{C}_{aibjck}}{\mathbf{M}_{ai} \mathbf{M}_{bj} \cdot \mathbf{M}_{ck} \mathcal{C}_{aibjck}^{\max}}, \quad (20)
 \end{aligned}$$

where $\mathcal{L}_{aibj}^{\max} = 0$ if C_{ab} or \bar{C}_{ij} is missing, or 1 otherwise; $\mathcal{C}_{aibjck}^{\max} = 0$ if C_{ab} , C_{bc} , \bar{C}_{ij} , \bar{C}_{jk} , S_{abc} or \bar{S}_{ijk} is missing, or 1 otherwise. Mis-matches in the slacks of \mathbf{M} are penalized with compatibility 0. This new design ensures $0 \leq E^n \leq 1$. We use E in the \mathcal{GA} matching process and use E^n for the final similarity computation.

We note that E^n is used only to estimate the final similarity but not in the \mathcal{GA} algorithm, due to an undesired increase in mathematical complexity. Recall that the \mathcal{GA} relies on a differential movement to migrate a doubly stochastic matrix into a discrete assignment matrix. The energy defined in Eq. (18) allows for a straightforward differentiation, where in Eq. (20) the differentiation introduces further complexity in the denominators.

7. Results and discussions

We perform an initial experiment on a human wrist bone dataset (courtesy of Dr. Crisco, RI Hospital [47]) to examine the shape

variations of the carpal bones across patients. The purpose of this experiment is to examine the alignment of bones based on the alignment of their \mathcal{MS} hypergraphs. In Fig. 10, the left-hand *hamates* of six females are matched against each other. Note that graph matching in this case is challenging because the regularized \mathcal{MS} hypergraphs contain large topological variations: One bone could contain only eight nodes, 10 curves, and three sheets, while another could contain 80 nodes, 105 curves, and 26 sheets. The proposed \mathcal{GA} matching maps most mismatches into the slacks, leading to many correct matches. We observe *asymmetry* matching results due to the rounding of \mathbf{M} into discrete assignments. The failure cases are mainly due to large unrecoverable structural variations. In general, our approach aligns shapes from the same category well, pointing a way potentially for structural shape variation studies.⁸

We have also tested our matching approach for object recognition and indexing on a small database (Fig. 11) composed of 20 shapes from five categories. The synthetic shapes are chosen to examine the matching across particular \mathcal{MS} transitions in isolation [15]. We also added a hand model collected online (from

⁸ Some implementation details: In handling the scale difference between shapes, we scale all shapes properly (to be with the same variance) in the pre-processing step prior to the matching. After the matching, a Euclidean transform is performed to align the two objects together for visualization. We color the matching nodes and curves and draw the unmatched ones in gray.

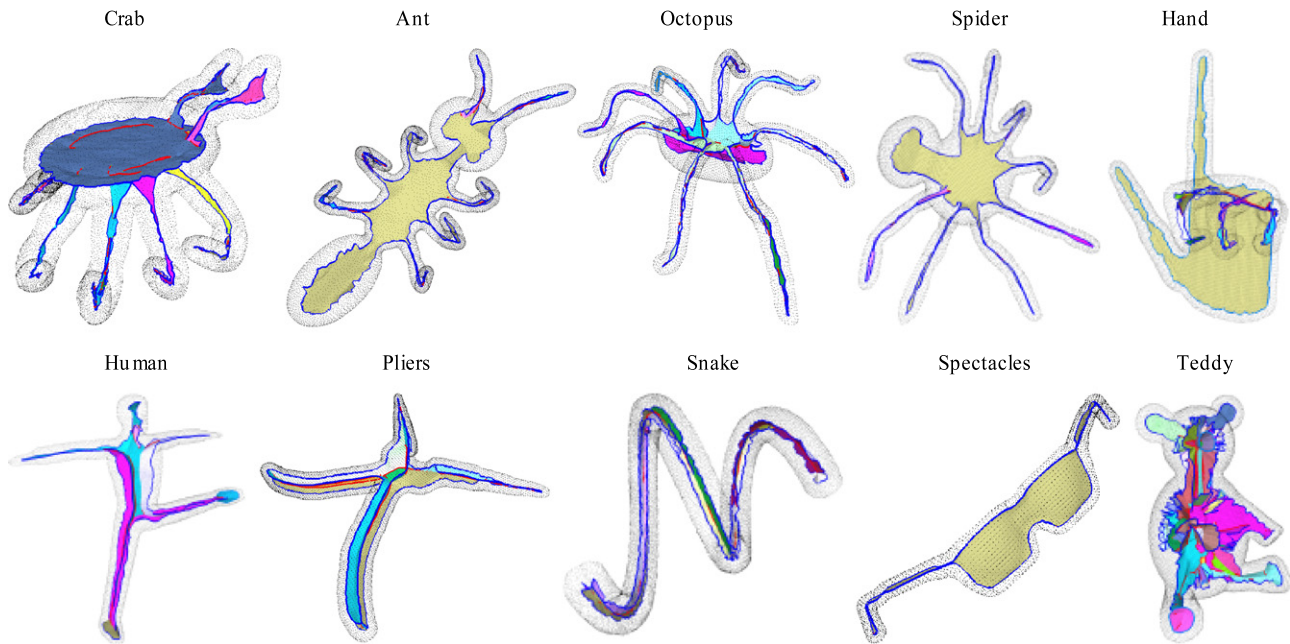


Fig. 12. The regularized \mathcal{MS} computed for an example shape in each category of the SHREC'10 dataset [45].

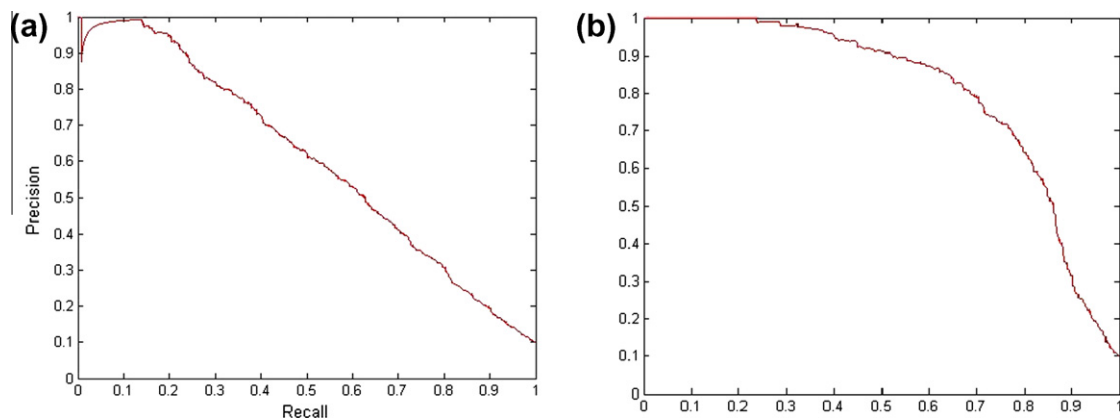


Fig. 13. The Precision-Recall (PR) curve for the SHREC'10 dataset from [45] (a) using all 10 categories and (b) using selected seven categories out of 10, excluding the ants, octopuses, and spiders which are overall similar to the crabs. This shows that most of the errors in (a) arise from the very similar categories.

Polhemus) with other hands generated from laser scans. Note that similarity measures of within-category shapes are much higher than non-category shapes, indicating the potential in applications such as shape retrieval and recognition. This experiment also validates the robustness of our method against noise and slight perturbation. The rectangular boxes and parabolic gutter shapes are perturbed with bumps (noise) and our method matches them robustly.

We have further evaluated our method using the SHREC'10 non-rigid 3D shape dataset [45],⁹ which contains 200 shapes from 10 categories. Note that the SHREC'10 dataset contains updated, refined subset of the McGill 3D Shape Benchmark [60]¹⁰ with equal number of models in each class. It also comes with more recent retrieval results comparing several methods [45]. We found that most of the shapes in the SHREC'10 dataset (as well the McGill dataset) contain voxelization artifacts resulting in grid like surfaces, which cause noisy \mathcal{MS} boundaries, or more precisely, zig-zag A_3 curves

[30]. We handle this by smoothing the polygonal mesh of each shape. We found that Guennebaud *et al.*'s Algebraic Point Set Surface (APSS) using Moving Least-Squares (MLS) projection [33] works effectively in removing these artifacts while preserving local features without shrinkage.¹¹ We then compute the \mathcal{MS} for each shape and manually tune for the best parameters in regularizing the \mathcal{MS} . Fig. 12 shows the regularized \mathcal{MS} of an example shape in each category of the SHREC'10 dataset.¹²

Observe that the ten selected categories are not equidistant from each other. The categories crab, ant, spider and octopus are structurally very similar: They all have a body and multiple limbs (legs and antennas). These four categories are perceptually much

¹¹ An implementation of the APSS MLS smoothing is made available in MeshLab (<http://meshlab.sourceforge.net/>).

¹² Our \mathcal{MS} regularization algorithm generally works with default parameters which are evaluated automatically for each shape [17,15]. However in dealing with unorganized point samples which could be arbitrary, two parameters are important: (1) the minimum radius λ which defines the boundary of a medial sheet at an A_3 curve. (2) a threshold that determines to what extent a leaf shock sheet (tab) should be kept or pruned (by a splice transform) [15].

⁹ <http://www.itl.nist.gov/iad/vug/sharp/contest/2010/NonRigidShapes/index.html>

¹⁰ <http://www.cim.mcgill.ca/shape/benchMark/>

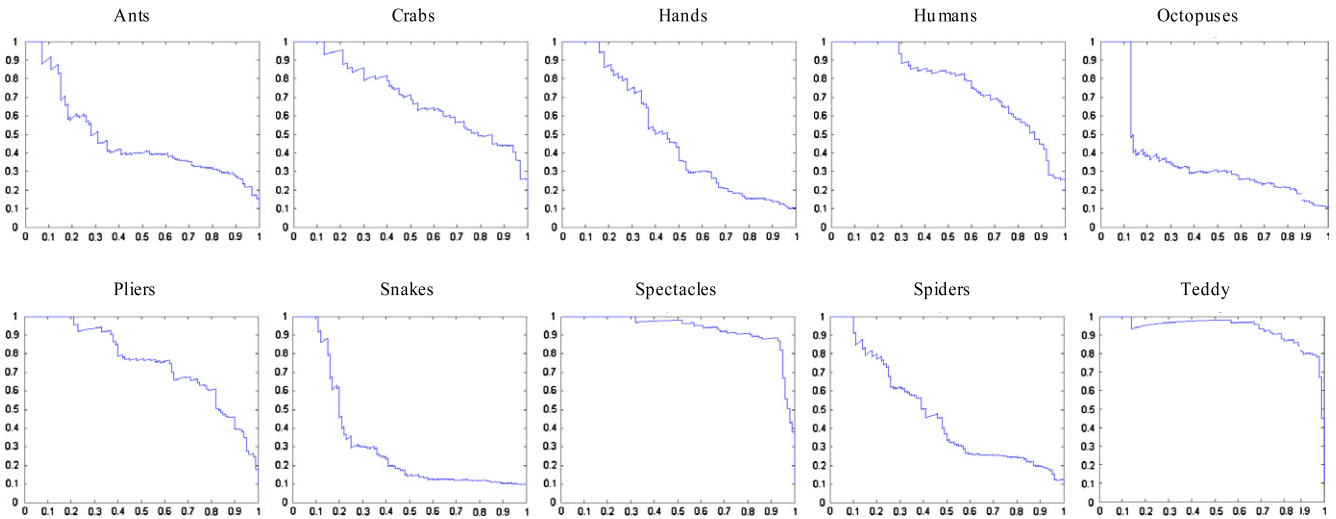


Fig. 14. The Precision-Recall (PR) curve for the query of shapes in the 10 categories of the SHREC'10 dataset [45].

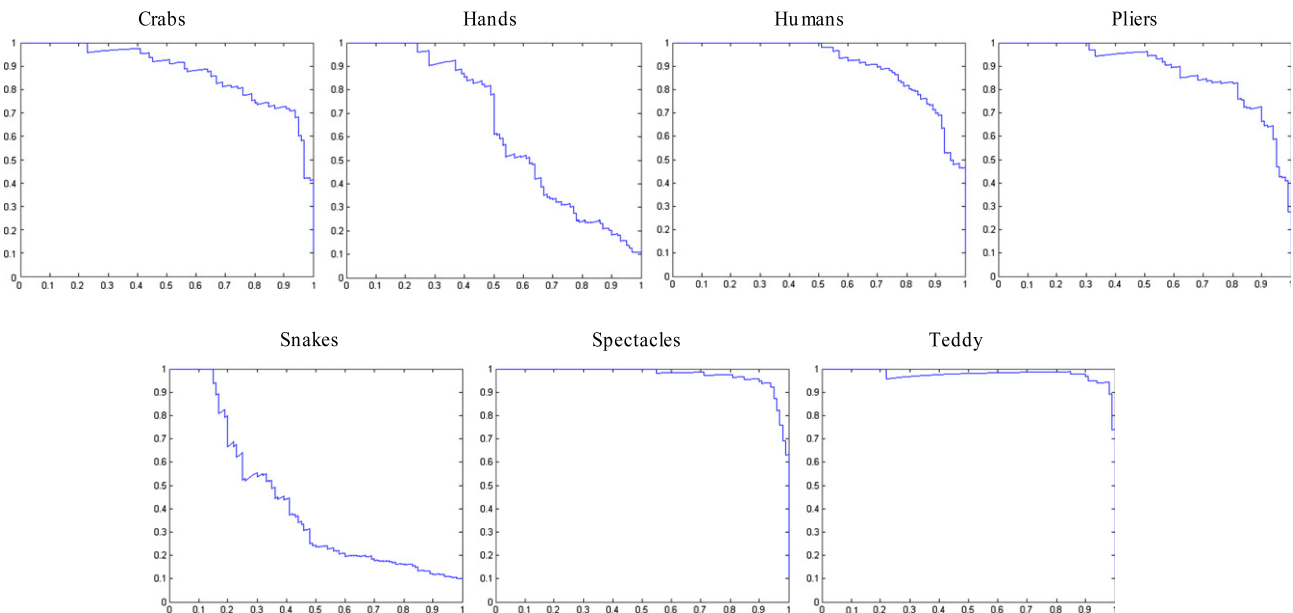


Fig. 15. The Precision-Recall (PR) curve for the query of shapes in the selected seven categories of the SHREC'10 dataset [45]. Observe how the performance increases by removing the ambiguous categories.

closer to each other than they are to other categories. Since our approach focuses on matching such topological level description of a shape, e.g., “body + eight limbs”, it is expected to more easily confuse these closer categories than a crab and a pair of spectacles. Thus, in using this particular database, we repeated on both the original database with the expected categorization as well as the case where the four very close categories are combined or three of the four removed.

The Precision-Recall (PR) curve for shapes for all categories in SHREC'10 is shown in Fig. 13a, while the PR for individual categories are in Fig. 14. As observed above, the selected category are not uniformly distinct from each other with four categories extremely close from the remaining six. Thus, to examine the performance when categories are more uniformly selected, we form a dataset of seven categories by omitting the ants, octopuses, and spiders and re-evaluate the PR curve in Figs. 13b and 15. Observe how the performance boosts by removing these very close categories.

Our method performed particularly well for the spectacles and teddy due to the uniqueness in categories. The performance for the snake category is poor because of by their highly singular symmetry—the instabilities of the \mathcal{MS} of such generalized cylinder like shapes (A_1^∞) are difficult to regularize. Similar phenomena are also observed in the fingers of the hands, but not in the rectangular handles of the pliers. In comparing to Siddiqi *et al.*'s medial surface retrieval method reported over the McGill 3D shape benchmark [60], our result is comparable and slightly better in some categories (spectacles, pliers, and the teddy) by visual examination of the PR curves; further investigation over the same baseline is required.

We discuss two sources of errors in our matching approach. (1) First, the \mathcal{GA} graph matching which essentially follows a greedy energy minimization scheme could lead to erroneous local solutions. (2) Second, un-regularized \mathcal{MA} instabilities could degrade the matching. By explicit regularization and matching to the 3rd

order and some further exploration by using the virtual links, we have reduced the effect of \mathcal{MA} instabilities, however there might be remaining \mathcal{MA} instabilities that potentially hinder us from accessing the coherence of shape and thus degrade the matching. Again we note that the ideal solution is to treat \mathcal{MA} instabilities as transitions of shapes and associate a proper distance/cost for each transition (as shown in Fig. 5). Here we approximate the ideal solution by first performing all regularizations and performing matching to calculate a total dissimilarity, expect errors due to the approximation.

Our method relies on two approaches to maintain robustness against sampling noise and resolution. First the \mathcal{MS} regularization exploits the transitions to ease sampling variations in extracting the \mathcal{MS} . We observed that \mathcal{MS} of slightly perturbed shapes does not vary much in most of our experiments. Second, the virtual links deal with some un-handled \mathcal{MS} transitions. The remaining even larger shape dissimilarities will be penalized when we match shapes in computing the compatibilities. We note that the matching robustness against noise and slight perturbation could be viewed as a sub-problem of matching shape across large variations and across categories. Refer to Fig. 5, distance d between shapes with slight perturbation is always smaller than matching shape with large variations. The computation in our matching process consists of two main parts: (1) computing the compatibilities between \mathcal{MS} nodes, links, corners, and (2) performing \mathcal{GA} hypergraph matching. The execution speed is then depending on the complexity of the \mathcal{MS} hypergraphs (number of nodes, links, sheets) that are given to the match engine. Generally we observe one to several minutes in matching two \mathcal{MS} hypergraphs of tens and hundreds of nodes/curves/sheets on a computer with 3GHz CPU and 2GB RAM.

The introduction of the 3rd-order energy makes the complexity of Eq. (18) to be $O(A^3I^3)$, where A, I are the numbers of nodes in the \mathcal{MS} . However such cubical term does not affect the computation time too much due to an efficient encoding of sparsity. We also note another importance of the sparsity as follows. The sparsity of the assignment matrix \mathbf{M} and the compatibility matrices $(\mathcal{N}, \mathcal{L}, \mathcal{C})$ keeps the computation numerically stable. Specifically, when we compute $\exp(1/T \cdot Q_{ai})$ in the pseudo code in Fig. 7 as we sum up the compatibilities and multiply it with \mathbf{M} as we decrease T , we need to ensure no exponential explosion in the numerical computations. This comes from a direct limitation of how many nodes (how large the graph) handle.

8. Conclusion

We have presented a medial axis based graph matching approach to measure 3D shape similarity by matching their \mathcal{MS} hypergraphs. Similarity is measured by a weighted sum of hypergraph compatibilities. Experimental results on medical shapes and a publicly available SHREC'10 dataset are reported, which suggests that a simple matching procedure over the regularized hypergraphs provides a way to distinguish categories. This is the first attempt exploiting the \mathcal{MA} transitions [31] integrated with a hypergraph matching framework. Our method is one of a few that is capable to match partial, non-closed, sampled shapes.

Future Directions: Several future directions are favorable. First, we expect additional \mathcal{MS} attributes such as the shock radius flow should provide valuable information in identifying important curves that are useful in matching. The shock flow field also provides a way to match the interior of the medial sheets, which are not yet exploited in this paper. Second, in addition to the graph-matching scheme, the \mathcal{MS} as a shape representation (feature) can be used in conjunction with other retrieval methods. Third, the proposed method is suitable for matching articulated

3D shapes. We expect to exploit its potential in matching articulated human shapes in 3D video applications [35].

Acknowledgments

This material is based upon work partly supported by the National Science Foundation under Grants NSF/IIS-0413215 and NSF/ITR-0205477. We gratefully acknowledge the SHREC'10 team in sharing their non-rigid 3D dataset. We also gratefully acknowledge the Shape Analysis Group in McGill University in providing the McGill 3D Shape Benchmark. We appreciate the MeshLab developers in sharing their software.

References

- [1] H.A. Almomahad, S.O. Duffuaa, A linear programming approach for the weighted graph matching problem, *PAMI* 15 (5) (1993) 522–525.
- [2] M. Ankerst, G. Kastenmüller, H.-P. Kriegel, T. Seidl, 3D shape histograms for similarity search and classification in spatial databases, in: *Symposium on Advances in Spatial Databases*, 1999, pp. 207–226.
- [3] T.F. Ansary, M. Daoudi, J.-P. Vandebror, A bayesian 3-d search engine using adaptive views clustering, *IEEE Transactions on Multimedia* 9 (2008) 78–88.
- [4] D. Attali, J.-D. Boissonat, H. Edelsbrunner, Stability and computation of the medial axis, in: *Mathematical Foundations of Scientific Visualization, Computer Graphics, and Massive Data Exploration*, 2004.
- [5] S. Belongie, J. Malik, J. Puzicha, Shape matching and object recognition using shape contexts, *IEEE Transactions on Pattern Analysis and Machine Intelligence (PAMI)* 24 (4) (2002) 509–522.
- [6] H.M. Berman, J. Westbrook, Z. Feng, G. Gilliland, T.N. Bhat, H. Weissig, I.N. Shindyalov, P.E. Bourne, The protein data bank, *Nucleic Acids Research* 28 (1997) 235–242.
- [7] D. Bespalov, W.C. Regli, A. Shokoufandeh, Reeb graph based shape retrieval for CAD, in: *Proceedings of ASME Design Engineering Technical Conference (DETC)*, 2003, pp. 1–10.
- [8] D. Bespalov, A. Shokoufandeh, W.C. Regli, W. Sun, Scale-space representation and classification of 3D models, *Journal of Computing and Information Science in Engineering* 3 (2003) 315–324.
- [9] S. Biasotti, D. Giorgi, M. Spagnuolo, B. Falcidieno, Reeb graphs for shape analysis and applications, *Theoretical Computer Science* 392 (1–3) (2008) 5–22.
- [10] S. Biasotti, S. Marini, M. Mortara, G. Patane, M. Spagnuolo, B. Falcidieno, 3D shape matching through topological structures, *Discrete Geometry for Computer Imagery, Lecture Notes in Computer Science*, vol. 2886, 2003, pp. 194–203.
- [11] A. Blake, A. Zisserman, *Visual Reconstruction*, MIT Press, Cambridge, MA, 1987.
- [12] H. Blum, Biological shape and visual science, *Journal of Theoretical Biology* 38 (1973) 205–287.
- [13] B. Bustos, D.A. Keim, D. Saupe, T. Schreck, D.V. Vranić, Feature-based similarity search in 3D object databases, *ACM Computing Surveys* 37 (4) (2005) 345–387.
- [14] M.-C. Chang, *The Medial Scaffold for 3D Shape Modeling and Recognition*, Ph.D. dissertation, Division of Engineering, Brown University, Providence RI, 2008.
- [15] M.-C. Chang, B. Kimia, Regularizing 3D medial axis using medial scaffold transforms, in: *Proceedings of IEEE CVPR*, 2008, pp. 1–8.
- [16] M.-C. Chang, F. Leymarie, B. Kimia, 3D shape registration using regularized medial scaffolds, in: *Proceedings of IEEE 3DPVT*, 2004, pp. 987–994.
- [17] M.-C. Chang, F.F. Leymarie, B.B. Kimia, Surface reconstruction from point clouds by transforming the medial scaffold, *Computer Vision and Image Understanding* 113 (November) (2009) 1130–1146.
- [18] D.-Y. Chen, X.-P. Tian, Y.-T. Shen, M. Ouhyoung, On visual similarity based 3D model retrieval, in: *Proceedings of the Eurographics, Granada, Spain*, 2003, pp. 223–232.
- [19] D. Conte, P. Foggia, C. Sansone, M. Vento, Thirty years of graph matching in pattern recognition, *IJPRAI* 18 (3) (2004) 265–298.
- [20] N.D. Cornea, M.F. Demirci, D. Silver, A. Shokoufandeh, S.J. Dickinson, P.B. Kantor, 3D object retrieval using many-to-many matching of curve skeletons, in: *SMI*, 2005, pp. 366–371.
- [21] N.D. Cornea, P. Min, Curve-skeleton properties, applications, and algorithms, *IEEE Transactions on Visualization and Computer Graphics* 13 (3) (2006) 530–548.
- [22] N.D. Cornea, D. Silver, R. Balasubramanian, Computing hierarchical curve-skeletons of 3D objects, *The Visual Computer* 21 (11) (2005) 945–955.
- [23] C.M. Cyr, B.B. Kimia, 3D object recognition using shape similarity-based aspect graph, in: *Proceedings of the IEEE International Conference on Computer Vision (ICCV)*, 2001, pp. 254–261.
- [24] T.K. Dey, J. Sun, Defining and computing curve-skeletons with medial geodesic function, in: *Proceedings of the Eurographics/ACM SIGGRAPH Symposium on Geometry Processing (SGP)*, Eurographics Association, 2006, pp. 143–152.
- [25] T. Funkhouser, M. Kazhdan, Shape-based retrieval and analysis of 3D models, in: *ACM SIGGRAPH Course Notes*, 2004, p. 16.

- [26] T. Funkhouser, P. Min, M. Kazhdan, J. Chen, A. Halderman, D. Dobkin, D. Jacobs, A search engine for 3D models, *ACM Transactions on Graphics* 22 (1) (2003) 83–105.
- [27] T. Furuya, R. Ohbuchi, Dense sampling and fast encoding for 3D model retrieval using bag-of-visual features, in: *The CIVR*, ACM, 2009, pp. 1–8.
- [28] R. Gal, D. Cohen-Or, Salient geometric features for partial shape matching and similarity, *ACM Transactions on Graphics* 25 (1) (2006) 130–150.
- [29] P. Giblin, B. Kimia, On the intrinsic reconstruction of shape from its symmetries, *PAMI* 25 (7) (2003) 895–911.
- [30] P. Giblin, B. Kimia, A formal classification of 3D medial axis points and their local geometry, *PAMI* 26 (2) (2004) 238–251.
- [31] P. Giblin, B. Kimia, Transitions of the 3D medial axis under a one-parameter family of deformations, *PAMI* 31 (5) (2009) 900–918.
- [32] S. Gold, A. Rangarajan, A graduated assignment algorithm for graph matching, *PAMI* 18 (4) (1996) 377–388.
- [33] G. Guennebaud, M. Germann, M.H. Gross, Dynamic sampling and rendering of algebraic point set surfaces, *Computer Graphics Forum* 27 (2008) 653–662.
- [34] M. Hilaga, Y. Shinagawa, T. Kohmura, T.L. Kunii, Topology matching for fully automatic similarity estimation of 3D shapes, in: *SIGGRAPH*, 2001, pp. 203–212.
- [35] P. Huang, A. Hilton, J. Starck, Shape similarity for 3d video sequences of people, *International Journal of Computer Vision* 89 (2–3) (2010) 362–381.
- [36] R. Hummel, S.W. Zucker, On the foundations of relaxation labeling processes, *PAMI* 6 (1983) 267–287.
- [37] C.Y. Ip, S.K. Gupta, Retrieving matching CAD models by using partial 3D pt. clouds, *CADA* 4 (2007) 629–638.
- [38] N. Iyer, S. Jayanti, K. Lou, Y. Kalyanaraman, K. Ramani, Shape-based searching for product lifecycle applications, *Computer-Aided Design* 37 (2005) 1435–1446.
- [39] A.E. Johnson, M. Hebert, Using spin images for efficient object recognition in cluttered 3D scenes, *PAMI* 21 (5) (1999) 433–449.
- [40] M. Kazhdan, T. Funkhouser, S. Rusinkiewicz, Rotation invariant spherical harmonic representation of 3D shape descriptors, in: *SGP*, 2003, pp. 156–164.
- [41] M. Kortgen, G.-J. Park, M. Novotni, R. Klein, 3D shape matching with 3D shape contexts, in: *CESCG*, 2003.
- [42] E. Lawler, D. Wood, Branch and bound methods: a survey, *Operations Research* 14 (1966) 699–719.
- [43] S. Lee, S. Yoon, I.D. Yun, D.H. Kim, K.M. Lee, S.U. Lee, A new 3-D model retrieval system based on aspect-transition descriptor, in: *ECCV*, 2006, pp. 543–554.
- [44] F. Leymarie, B. Kimia, The medial scaffold of 3D unorganized point clouds, *PAMI* 29 (2) (2007) 313–330.
- [45] Z. Lian, A. Godil, T. Fabry, T. Furuya, J. Hermans, R. Ohbuchi, C. Shu, D. Smeets, P. Suetens, D. Vandermeulen, S. Wuhrer, SHREC'10 track: non-rigid 3D shape retrieval, in: *Eurographics Workshop on 3D Object Retrieval*, 2010, pp. 1–8.
- [46] Y. Liu, H. Zha, H. Qin, The generalized shape distributions for shape matching and analysis, in: *SMI*, 2006, p. 16.
- [47] D.C. Moore, J.J. Crisco, T.G. Trafton, E.L. Leventhal, A digital database of wrist bone anatomy and carpal kinematics, *Journal of Biomechanics* 40 (11) (2007) 2537–2542.
- [48] R. Ohbuchi, T. Minamitani, T. Takei, Shape-similarity search of 3d models by using enhanced shape functions, in: *TPCG*, 2003, p. 97.
- [49] R. Osada, T. Funkhouser, B. Chazelle, D. Dobkin, Shape distributions, *ACM Transactions on Graphics* 21 (4) (2002) 807–832.
- [50] P. Papadakis, I. Pratikakis, S. Perantonis, T. Theoharis, Efficient 3D shape matching and retrieval using a concrete radialized spherical projection representation, *Pattern Recognition* 40 (2007) 2437–2452.
- [51] A. Rangarajan, E. Mjolsness, A Lagrangian relaxation network for graph matching, *ICNN* 7 (1994) 4629–4634.
- [52] D. Saupe, D.V. Vranic, 3D model retrieval with spherical harmonics and moments, in: *FSDAGM*, 2001, pp. 392–397.
- [53] R. Schnabel, R. Wahl, R. Wessel, R. Klein, Shape recognition in 3D point clouds, Technical report, Univ. Bonn., 2007.
- [54] T. Sebastian, P. Klein, B. Kimia, On aligning curves, *PAMI* 25 (1) (2003) 116–125.
- [55] T. Sebastian, P. Klein, B. Kimia, Recognition of shapes by editing their shock graphs, *PAMI* 26 (2004) 551–571.
- [56] D. Sharvit, J. Chan, H. Tek, B.B. Kimia, Symmetry-based indexing of image databases, *JVCIR* 9 (4) (1998) 366–380.
- [57] J.-L. Shih, C.-H. Lee, J.T. Wang, A new 3D model retrieval approach based on the elevation descriptor, *Pattern Recognition* 40 (1) (2007) 283–295.
- [58] A. Shokoufandeh, D. Macrini, S. Dickinson, K. Siddiqi, S.W. Zucker, Indexing hierarchical structures using graph spectra, *PAMI* 27 (7) (2005) 1125–1140.
- [59] K. Siddiqi, S. Pizer (Eds.), *Medial Representations: Mathematics, Algorithms and Applications*, Kluwer Academic Publishers, 2009.
- [60] K. Siddiqi, J. Zhang, D. Macrini, A. Shokoufandeh, S. Bouix, S. Dickinson, Retrieving articulated 3-D models using medial surfaces, *Machine Vision and Applications* 19 (2008) 261–275.
- [61] P.D. Simic, Constrained nets for graph matching and other quadratic assignment problems, *Neural Computation* 3 (1991) 268–281.
- [62] R. Sinkhorn, A relationship between arbitrary positive matrices and doubly stochastic matrices, *Annals of Mathematical Statistics* 35 (1964) 876–879.
- [63] D. Smeets, T. Fabry, J. Hermans, D. Vandermeulen, P. Suetens, Isometric deformation modelling for object recognition, in: *CAIP*, Springer-Verlag, 2009, pp. 757–765.
- [64] M. Styner, G. Gerig, S. Joshi, S. Pizer, Automatic and robust computation of 3D medial models incorporating object variability, *IJCV* 55 (2–3) (2003) 107–122.
- [65] H. Sundar, D. Silver, N. Gagvani, S. Dickinson, Skeleton based shape matching and retrieval, in: *SMI*, 2003, pp. 130–139.
- [66] J.W.H. Tangelder, R.C. Veltkamp, A survey of content based 3D shape retrieval methods, in: *SMI*, 2004, pp. 145–156.
- [67] S. Umeyama, An eigendecomposition approach to weighted graph matching problems, *PAMI* 10 (September) (1988) 695–703.
- [68] E.H. Weber, *De pulsu, resorptione, audita et tactu, Annotationes anatomicae et physiologicae*, Koehler, Leipzig, 1834.
- [69] G.V. Wilson, G.S. Pawley, On the stability of the traveling salesman problem algorithm of hopfield and tank, *Biological Cybernetics* 58 (1988) 63–70.
- [70] S. Wuhrer, C. Shu, Z.B. Azouz, P. Bose, Posture invariant correspondence of incomplete triangular manifolds, *International Journal of Shape Modeling* 13 (2007) 139–157.